

Review

Photoacoustic Imaging of Human Skin for Accurate Diagnosis and Treatment Guidance

Yue Ying¹, Hong Zhang^{1,2,*} and Li Lin^{1,3,*}¹ College of Biomedical Engineering and Instrument Science, Zhejiang University, Hangzhou 310027, China; 22260309@zju.edu.cn² The Second Affiliated Hospital, Zhejiang University School of Medicine, Hangzhou 310009, China³ The First Affiliated Hospital, Zhejiang University School of Medicine, Hangzhou 310003, China

* Correspondence: hzhang21@zju.edu.cn (H.Z.); linliokok@zju.edu.cn (L.L.)

Abstract: Photoacoustic imaging (PAI) is a cutting-edge biomedical imaging modality, providing detailed anatomical and functional information about the area beneath the skin surface. Its light energy deposition is such that PAI typically provides clear images of the skin with high signal-to-noise ratios. Specifically, the rich optical contrast of PAI allows biological information related to lesion growth, malignancy, treatment response, and prognosis to be seen. Given its significant advantages and emerging role in imaging skin lesions, we summarize and comment on representative studies of skin PAI, such as the guidance of skin cancer biopsies and surgical excisions, and the accurate diagnosis of psoriasis. We conclude with our insights about the clinical significance of skin PAI, showing how its use to identify biological characteristics in lesion microenvironments allows early diagnosis and prognosis of disease.

Keywords: photoacoustic imaging; skin cancer; psoriasis; diagnosis; treatment guidance



Citation: Ying, Y.; Zhang, H.; Lin, L. Photoacoustic Imaging of Human Skin for Accurate Diagnosis and Treatment Guidance. *Optics* **2024**, *5*, 133–150. <https://doi.org/10.3390/opt5010010>

Academic Editors: Thomas Seeger and Francesco Chiavaioli

Received: 21 January 2024

Revised: 18 February 2024

Accepted: 26 February 2024

Published: 1 March 2024



Copyright: © 2024 by the authors. Licensee MDPI, Basel, Switzerland. This article is an open access article distributed under the terms and conditions of the Creative Commons Attribution (CC BY) license (<https://creativecommons.org/licenses/by/4.0/>).

1. Introduction

Skin diseases are complex and widespread. They include inflammatory, infectious, autoimmune, neoplastic, and genetic skin diseases with different origins, symptoms, and severity. As a consequence, accurate diagnosis is essential to achieve effective treatment with appropriate patient management. Misdiagnosis may lead to ineffective therapy, unnecessary side effects, or erroneous treatment. Accordingly, a high-resolution, informative, and safe imaging modality is preferred to provide accurate diagnosis and treatment feedback for improved patient management [1].

Accurate skin disease diagnosis and treatment assessment require sensitive imaging of the lesion's anatomical and pathological information with high spatiotemporal resolution. Multiple imaging modalities have been developed for such goals, including dermoscopy [2,3], confocal microscopy [4,5], optical coherence tomography (OCT) [6,7], and ultrasound [8]. In general, optical microscopy offers high spatial resolutions, making it ideal for the detailed examination of superficial skin structures and cellular morphology. However, its capability to penetrate beyond the epidermis is limited by the ballistic regime of light, typically reaching depths of only about 1 mm. As a result, optical microscopy is best suited for analyzing thin and superficial lesions, where the pathology predominantly resides within the epidermal layers [9,10]. While optical microscopy excels in providing detailed imaging of superficial structures, it faces challenges in assessing deeper layers of the skin, including the papillary dermis and beyond. This limitation hinders a comprehensive evaluation of lesions with abnormalities in the deeper layers, such as microvascular anomalies within the dermis or the measurement of tumor thickness, which is crucial for staging and prognostic assessment in various skin cancers. Ultrasonography is advantageous in skin imaging due to its ability to penetrate deeper layers of tissue compared to optical microscopy, providing valuable morphological information [11]. It excels in

assessing structural changes within the skin, such as alterations in dermal thickness, and can accurately measure parameters like tumor thickness, aiding in disease staging and treatment planning. However, one significant drawback is its inability to directly measure microvascular abnormalities within the skin. While it can visualize larger blood vessels and assess blood flow characteristics, its spatial resolution is insufficient to detect and quantify microvascular changes. Furthermore, ultrasonography may lack specificity in identifying certain pathological features or molecular alterations underlying skin diseases. It primarily provides anatomical information and may not be able to differentiate between benign and malignant lesions solely based on morphological characteristics. Therefore, ultrasonography may need to be complemented with other imaging modalities or histopathological analysis for the comprehensive evaluation of skin conditions. Each imaging technique has certain advantages and limitations (Table 1). Skin imaging therefore requires a modality complementary to these existing techniques, to bridge between the microscopic and macroscopic scales with rich optical contrast.

Table 1. Comparison of PAI and other imaging modalities.

Imaging Modality	Sensitivity	Resolution	Imaging Depth
Photoacoustic Imaging	High sensitivity to endogenous chromophores such as hemoglobin and melanin, enabling detection of subtle changes in tissue oxygenation and vascularization.	High spatial resolution, typically ranging from tens to hundreds of micrometers, enabling detailed imaging of skin structures including blood vessels, pigmented lesions, and subcutaneous.	Penetrates several millimeters beneath the skin surface, providing information about structures located deeper in the tissue.
Dermoscopy	High sensitivity to surface features and pigmented lesions, aiding in the detection of melanoma and other skin cancers.	Provides magnified views of skin lesions with detailed surface characteristics, such as pigment patterns, vascular structures, and specific dermal structures.	Limited to superficial layers of the skin, providing surface-level information about skin lesions.
Confocal Microscopy	Cellular-level sensitivity, visualizing individual skin cells, nuclei, and cellular organelles.	Sub-cellular resolution, providing detailed morphological information about cellular architecture and identifying cellular abnormalities associated with skin diseases.	Limited to superficial layers of the skin, typically up to 100–200 μm deep, depending on the imaging system and objective used.
Optical Coherence Tomography	High sensitivity to changes in tissue optical scattering properties, providing detailed cross-sectional images of skin layers.	Micrometer-scale resolution, providing detailed imaging of skin layers and fine structural features such as epidermal-dermal junctions, hair follicles, and sweat glands.	Penetrates up to 1–2 mm into the skin, depending on the wavelength of light used and tissue scattering properties.
Ultrasound	Excellent sensitivity to tissue density variations, detecting structural abnormalities such as tumors, cysts, and edema.	Spatial resolution on the order of millimeters, allowing visualization of macroscopic features such as tumor size, shape, and depth within the skin.	Penetrates several centimeters into the tissue, depending on the frequency of the ultrasound probe.

Photoacoustic imaging (PAI), also known as optoacoustic imaging, is a biomedical imaging modality that combines optical excitation and acoustic detection and which shows promise for fulfilling the above requirements [12–19]. PAI has been demonstrated to provide a scalable field of view (FOV), high spatiotemporal resolutions, and pathology-related imaging contrast without ionizing radiation or contrast agent injection. It uses a pulsed laser to irradiate biological tissues. The absorbed photons heat the biological chromophores instantaneously and generate a rise in pressure via transient thermoelastic expansion. The pressure rise then propagates outward in the form of ultrasonic waves

(photoacoustic waves), which suffer negligible scattering before being detected using ultrasonic transducers placed around the tissue. The amplitude of the pressure rise can then be calculated via image reconstruction algorithms, revealing the concentration and distribution of the chromophores beneath the skin surface [20–22]. The optical absorption-based contrast and the hybrid nature of PAI enables the acquisition of structural, functional, and molecular information with a high depth-to-resolution ratio [14,23,24].

In PAI, the high-optical contrast permits analysis of pathological characteristics with or without labeling, the high depth-to-resolution ratio allows clear visualization of detailed features from the epidermis to the dermis, and the high-imaging speed reduces motion artifacts and facilitates fast scanning. PAI therefore shows early promise for accurate diagnosis and treatment guidance of various skin diseases with improved patient management.

In this review, our objective is to narrow down the focus to the application of PAI in dermatology, a domain that has often been approached with a broader scope in previous literature [25–31]. Unlike previous reviews that predominantly focused on either photoacoustic microscopy (PAM) or photoacoustic computed tomography (PACT) [32–35], our review encompasses both modalities, offering a comprehensive overview of PAI applications in dermatology. By consolidating information on major PAI configurations and highlighting multiple clinical translation potentials, we aim to emphasize the unique role of PAI in addressing critical challenges in the diagnosis and treatment of skin cancer, psoriasis, and other dermatological conditions (Figure 1). This targeted approach allows for a deeper exploration of PAI's potential contributions to dermatology, enhancing the understanding of its clinical relevance and utility.

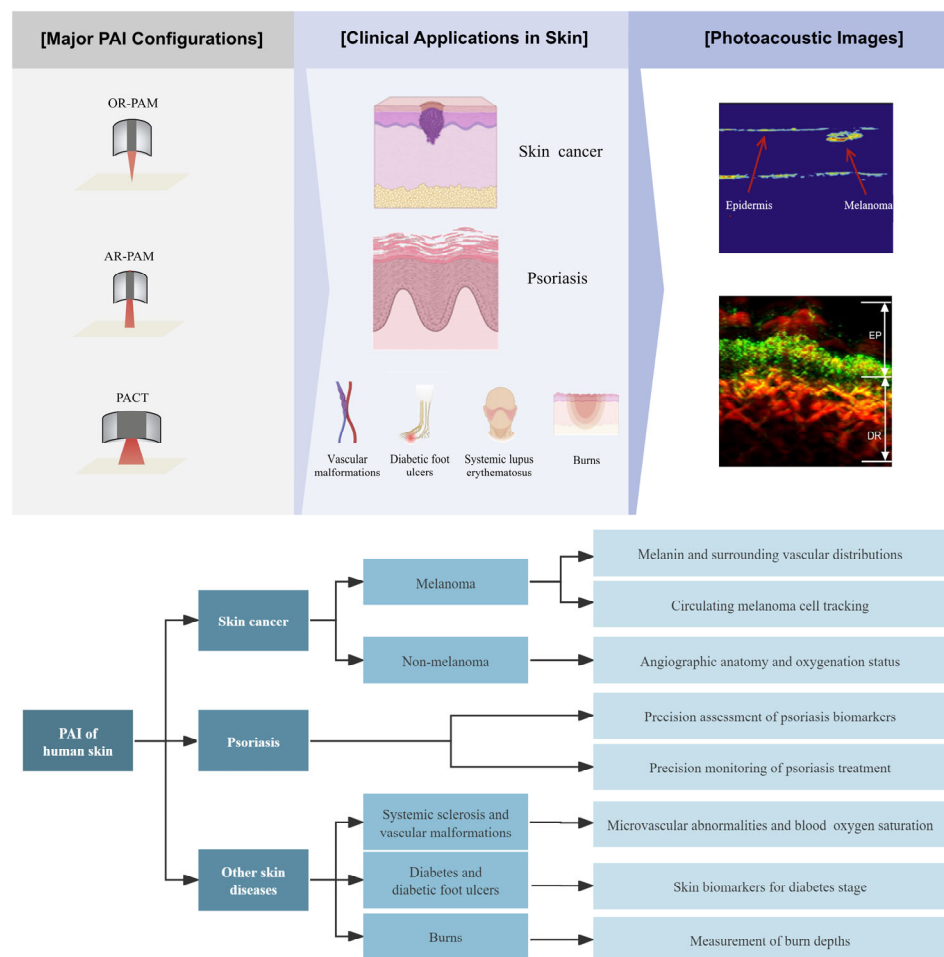


Figure 1. The application of PAI in dermatology.

2. Key Features of PAI

Most PAI systems can be classified into three categories according to their image formation approach: optical-resolution photoacoustic microscopy (OR-PAM) [36–38], acoustic-resolution photoacoustic mesoscopy (AR-PAM) [39–41], and PACT [42–45]. Specifically, OR-PAM relies on the rapid scanning of a tightly focused light beam to render optical-resolution images near the surface [46–48]. In comparison, AR-PAM scans a loosely focused light beam for excitation, but a focused ultrasound beam for detection [49,50]. In AR-PAM, the acoustic focus typically generates coarser lateral resolutions than the optical focus in OR-PAM, but generally images deeper than OR-PAM since ultrasound scatters much less than light in biological tissues [36,51–54]. For even deeper penetration, PACT usually uses expanded light beams to excite the tissue homogenously and detects PA waves using multiple ultrasonic transducers in parallel [55] (Figure 2a). Consequently, the images are reconstructed via acoustic inversion algorithms in the optical diffusive regime. All three PAI configurations make PAI scalable from epidermis to dermis with a high depth-to-resolution ratio (~200), thus bridging the longstanding gap between microscopic and macroscopic observations of skin (Table 2).

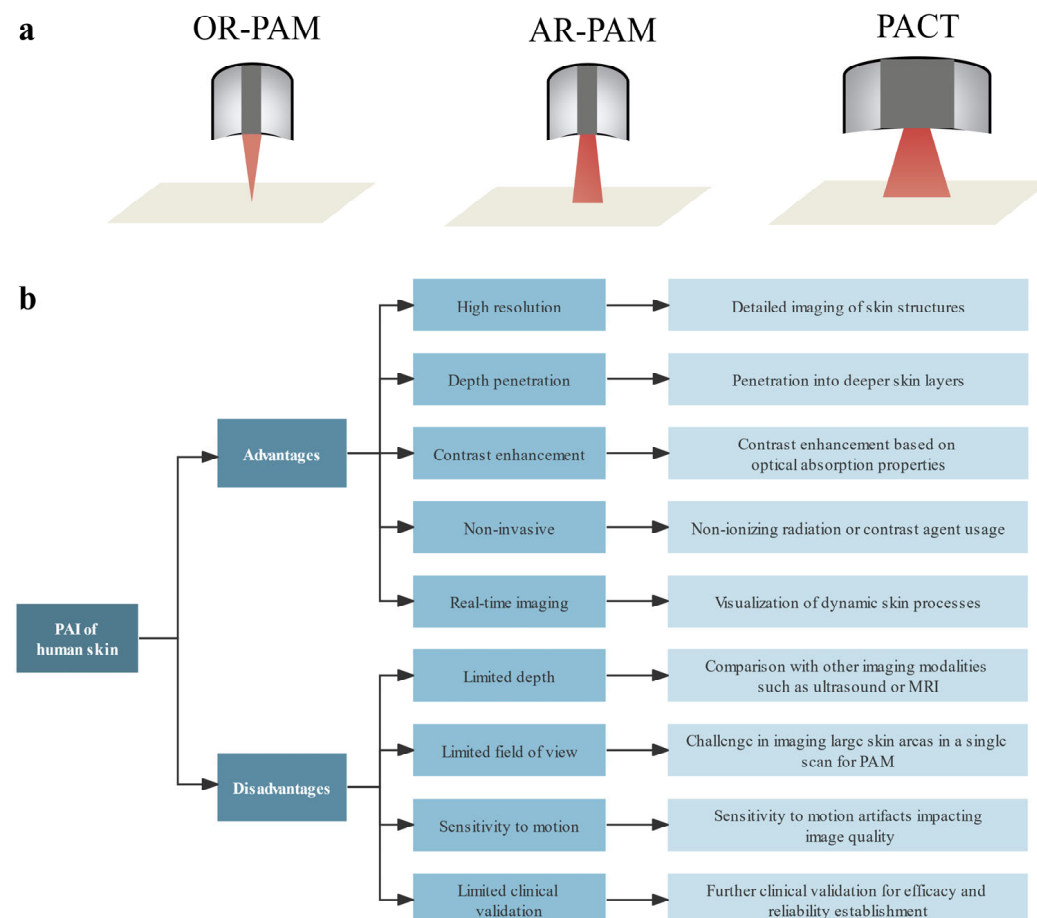


Figure 2. (a) Major implementation of PAI. (b) The advantages and disadvantages of PAI of human skin.

In photoacoustic imaging, key parameters significantly impact image quality and specificity [56–63]. Acoustic Frequency: typically ranges from a few to tens of megahertz. Higher frequencies (e.g., 10–50 MHz) offer finer spatial resolution (tens of micrometers), suitable for imaging superficial structures like skin layers and small blood vessels. Lower frequencies (e.g., 1–10 MHz) penetrate deeper (several millimeters to centimeters) but with reduced spatial resolution. Optical Wavelength: the choice depends on target tissue components. Near-infrared (NIR) wavelengths (700–1300 nm) are common for deep tissue imaging, due

to reduced scattering and absorption by hemoglobin and water. Shorter wavelengths (e.g., visible light) may be preferred for specific chromophores like melanin. Pulse Duration: typically ranges from picoseconds to microseconds. Shorter pulses (<10 nanoseconds) are preferred for high-resolution imaging, as they minimize motion artifacts and provide better temporal resolution. However, they require higher energy and may increase tissue damage risk. Longer pulses (>100 nanoseconds) are less energy intensive but may reduce spatial resolution. Polarization: while less quantifiable, polarization modulation enhances contrast and provides additional tissue structure information. Analyzing changes in light polarization before and after tissue interaction can differentiate between tissue components with different optical properties.

Table 2. Key features of the major configurations of PAI.

	OR-PAM	AR-PAM	PACT
Depth	<1.5 mm [46–48]	≤5 mm [49,50]	≤40 mm [20]
Penetrated skin layers	Epidermis and partially dermis	Epidermis, dermis, and subcutaneous tissue	Epidermis, dermis, and subcutaneous tissue
Resolution	Lateral: 0.3–5 μm Axial: 15–30 μm [64,65]	Lateral: 20–80 μm Axial: 20–60 μm [66]	30–400 μm [20,55]
Resolved features	Capillaries	Arterioles and venules	Arterioles, venules, and larger vessels
Frame rate	A few hertz [48,64,67]	Several tens of hertz [49,50]	Several tens or even hundreds of hertz [20,55]

The distinct absorption spectra of biological components allow PAI to reveal comprehensive information about the lesion. By scanning the excitation light through multiple wavelengths, PAI can image a variety of endogenous or exogenous absorbers, enabling the detection of anatomical, physiological, metabolic, molecular, and genetic events in the body [68–70]. The abundant imaging information allows PAI to detect the presence of specific biomolecules and pathological features, identifying the lesion's malignancy and progression [35,71–76]. The diagnostic capability of PAI can be further extended to the guidance of treatment and assessment of therapy, facilitating accurate and personalized treatment to treat skin cancer and psoriasis, as well as other skin diseases (Figure 2b).

High-imaging speed is critical for imaging living objects or dynamic biological processes. PAI can acquire images up to hundreds of frames per second, reducing motion-induced artifacts and improving imaging efficiency [77,78]. For example, PAI can scan a whole human breast within a single breath hold of 10 s [20]. Thus, high-imaging speed is one of the significant advantages of PAI, enabling real-time monitoring of biological processes *in vivo*.

3. Clinical Applications in Skin Imaging

Here, we focus on the PAI of the skin and present its studies aiming at fulfilling the clinical requirements in the diagnosis and treatment of skin cancer and psoriasis, among numerous skin diseases. For skin cancer diagnosis and treatment assessment, there has been significant research on the precise measurements of tumor thickness, as well as blood vasculatures and oxygenation states in the tumor microenvironment. Other than imaging solid tumors, PAI can detect circulating tumor cells, providing early promise in treatment assessment and prognosis. In addition to cancer imaging, PAI studies have paid special attention to psoriasis diagnosis, offering precise and objective evaluations.

3.1. Skin Cancer Imaging

3.1.1. PAI of Melanoma

Normal human skin is divided into three layers: epidermis, dermis, and subcutaneous tissue (Figure 3a). Melanocytes, located in the basal layer of the epidermis, are normal human cells which produce pigment and protect the skin from ultraviolet radiation. Melanoma, which is the deadliest form of skin cancer, arises from the malignant transformation of melanocytes [79]. Although it accounts for only 5% of skin cancers, melanoma is responsible for over 60% of skin cancer-related deaths [80–82].

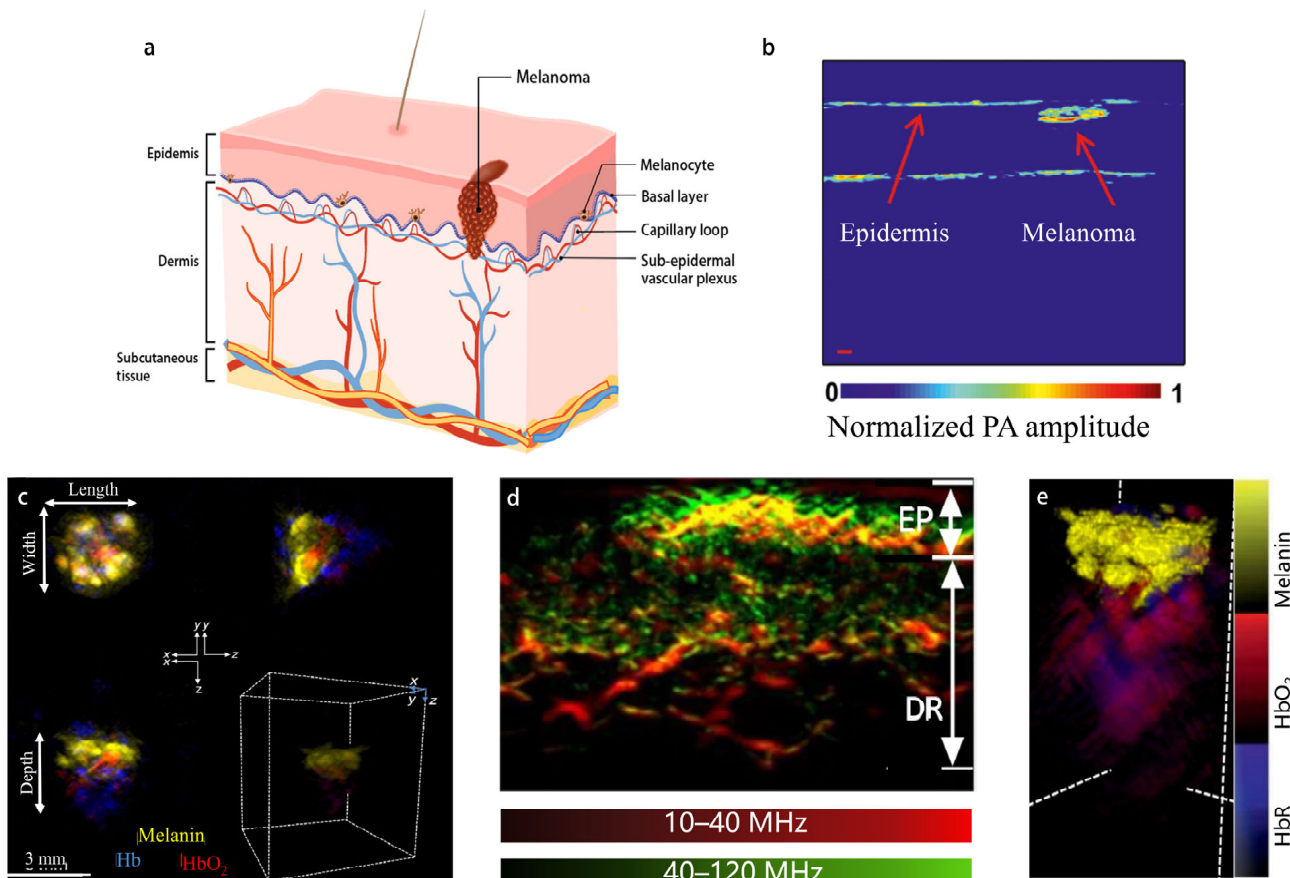


Figure 3. (a) Layers of human skin. (b) Melanoma image acquired with PACT, clearly showing the melanoma and skin surface [83]. (c) In vivo Volumetric Multispectral optoacoustic tomography (vMSOT) images in different orthogonal views and 3D map of skin tumor showing melanin, Hb (blue) and HbO₂ (red) signals. Clusters of melanin signals were observed with strong hemoglobin signals underneath the tumor, indicating the extent of tumor's vascularity. Measurements of tumor dimensions were acquired from the xy and xz planes to obtain the maximum length, width and depth (including vasculature) parameters [84]. (d) Maximum intensity projection (MIP) cross-sectional images of a melanoma lesion edge (red: larger structures in the bandwidth of 10–40 MHz; green: smaller structures in the bandwidth of 40–120 MHz) [85]. (e) 3D MSOT rendering of a representative BCC lesion showing melanin (yellow), Hb (blue) and HbO₂ (red) signals. Melanin signals were clustered at the top with strong hemoglobin signals underneath the BCC, showing deeper vasculature structures and the lesion [71].

Tumor thickness is an important indicator of melanoma progression and metastasis. Melanoma cells initially grow within the epidermis layer, in what is usually called the “horizontal growth phase”. Accurate diagnosis followed by extended surgical resection at this stage would remove tumor cells with minimal risk of recurrence. Without proper treatment, however, tumor cells will start to invade the dermis during the “vertical growth

phase". Blood and lymph vessels distributed in the dermis will facilitate melanoma cell metastasis, which may lead to fatality. Accordingly, tumor thickness is a key factor in staging melanoma, guiding treatment and assessing prognosis [80,86].

Accurate measurement of melanoma thickness remains a challenge in clinics due to the limited imaging depth of skin imagers and the low imaging contrast to reveal the lesions' pathological features. Currently, surgical excision biopsy with narrow margins and partial biopsy are typically applied for this purpose [87,88]. Although dermatology guidelines recommend biopsy from the irregular and hyperpigmented sections, insufficient sampling of the primary lesion limits the accuracy of partial biopsy [89]. Consequently, a comprehensive and precise measurement of melanin distribution and the melanoma microenvironment can improve early diagnosis and guidance in deciding the positions and depths of biopsies.

The high-optical contrast allows PAI to reveal the melanin content in melanoma cells beneath the epidermis. For example, Breathnach et al. developed a handheld PAI probe to measure melanoma thickness [90]. While the thickness of the lesions measured using PACT was highly correlated with histology ($r = 0.99, p < 0.001$ for melanoma, $r = 0.98, p < 0.001$ for nevi), the limited view of the linear ultrasonic array compromised the image clarity. Another linear array-based PACT system was used for melanoma measurement at depths ranging from 0.2 to 6.0 mm (Figure 3b) [83]. Probably due to the dehydration and shrinkage of histology samples, the system quantified a slightly thicker (around 13% thicker) tumor depth *in vivo* compared to histological measurements *ex vivo* [83,90]. The distinctive oxy-hemoglobin (HbO_2) and deoxy-hemoglobin (Hb) signals captured through PACT revealed vascular infiltration surrounding melanin-rich areas, providing additional features to diagnose the tumor's invasiveness [49,84,85,91–93] (Figure 3c).

In addition to the depth, blood vasculatures in the melanoma's microenvironment are closely associated with the invasiveness and metastatic stages of the tumor [94–96]. Accordingly, three-dimensional imaging of the vascular features across the skin layers can provide pathological details around the tumor which are inaccessible via traditional dermatoscopy. He et al. imaged microvessels throughout the skin to a depth of 1.5 mm at a wavelength of 532 nm within a single breath hold of 15 s, with a resolution of tens of micrometers (Figure 3d) [85]. *In vivo* images from 10 melanoma and 10 benign moles showed significant difference in microvasculatures (e.g., the dermal vasculature in the melanoma edge areas exhibited a significantly higher total blood volume and vessel density compared to the melanocytic nevus) between malignant and benign lesions, showing an early promise for diagnostic improvement.

Multiple PAI studies have demonstrated the measurement of melanoma depths with verified histopathological correlation. In addition, clear imaging of the homogeneous characteristics further facilitate the non-invasive assessment of the lesion's malignancy and invasiveness. Therefore, preoperative PAI of melanoma can be a useful tool for biopsy guidance, allowing more accurate sampling and eliminating the need for redundant biopsies.

3.1.2. Detection and Treatment of Circulating Melanoma Cells

Circulating melanoma cells (CMCs), an exclusive subset of circulating tumor cells [97], are melanoma cells that have detached from the tumor and circulated in the bloodstream. Since CMCs are critical indicators of tumor metastasis [98,99], the identification and quantification of CMCs are essential for the diagnosis and prognosis of the cancer. Existing techniques (such as immune-mediated assays and polymerase chain reaction) for CMC detection rely primarily on antigen–antibody recognition or physical properties of tumor cells, and suffer from inadequate sensitivity and specificity due to extremely low levels of CMCs in the blood [100,101].

To address this critical need, multiple PAI studies for CMC detection have been performed. One early stage study detected melanoma cells in human blood samples from a patient with stage-IV melanoma using a photoacoustic flowmetry system [102]. Multiple photoacoustic flow cytometry (PAFC) systems have been developed to enumerate

CMCs in early stage melanoma patients (I–III stages), showing a capability of detecting two CMCs/mL in human blood draws. Out of 27 patients (67%) with more than two CMCs/mL detected using the PAFC, 18 eventually developed metastatic diseases during their follow-up times [100]. In another study, a cytophone PAFC system was invented which detected CMCs in 27 of 28 of melanoma patients, yet reported zero CMC events in healthy participants [103]. Recently, a linear array-based PACT system has been optimized for the detection of CMCs subcutaneously in stage III–IV melanoma patients *in vivo*. Patients with positive test results had higher chances of disease progression in follow-up studies [104].

Moreover, PAFC holds promise for improving the prevention of metastatic disease through the targeted elimination of melanoma cells in circulation. A dual-wavelength PAFC has been developed, integrated with a melanoma-specific laser therapy mechanism [105]. The *in vivo* label-free imaging of CMCs in mice enabled the immediate initiation of a targeted laser treatment upon detection of the melanoma cell's photoacoustic signal. The melanoma cell was thermally destroyed without collateral damage [105].

3.1.3. Non-Invasive Tumor Margin Imaging of Non-Melanoma

Different from melanoma, non-melanoma skin cancers (NMSCs) typically exhibit less aggressiveness and lower metastatic tendencies, underscoring the crucialness of complete surgical excision [106]. However, accurate measurement of tumor size is critical for successful tumor resection. Accordingly, preoperative imaging is helpful to improve precise excisions by providing volumetric information about the melanin concentration and blood vasculature. Non-invasive preoperative imaging also aids in the delineation of tumor margins, minimizing the chance of incomplete excision. This imaging approach aligns seamlessly with Mohs surgery to shortening the operative procedures and improve the cost effectiveness [107].

NMSCs are often lightly pigmented and contain melanin, serving as an endogenous contrast agent for PAI. A recent study successfully distinguished NMSC tumors from normal skin in 21 Asian NMSC patients imaged using MSOT (Multispectral Optoacoustic Tomography), which analyzed the optical spectrum of the lesion (Figure 3e) [71]. Its real-time 3D imaging capability also allowed the visualization of the lesion's structures and associated vascular angiogenesis, which is a well-acknowledged indication of tumor invasiveness [108,109]. Another approach involves a planar-view PACT using a Fabry–Pérot interferometer (FPI) to provide higher acoustic detection performance than piezoelectric transducers [110]. The transparent FPI sensor also facilitates integration with other optical imaging modalities, such as OCT [111]. Proof-of-principle studies have demonstrated 3D imaging of a surgical scar and basal cell carcinoma in human skin. In addition to the anatomical imaging of NMSC-associated angiogenesis, multi-spectral PAI is capable of mapping oxygen saturation in tumor microenvironments to identify hypoxia-related malignancy biomarkers [112].

3.2. Psoriasis

Psoriasis is a chronic skin disease mainly characterized by the appearance of abnormal skin patches [113,114]. The histology of psoriatic skin exhibits hyperkeratosis, acanthosis, inflammatory cellular infiltrate, and modified microvascular architecture (Figure 4a). Clinics typically evaluate psoriasis via visual assessment based on the Psoriasis Area and Severity Index (PASI) scoring system. Although diagnostic accuracy is limited by the lack of subcutaneous information and by subjective judgment, the evolving understanding of this disease has made microvascular alterations become crucial pathophysiological markers in the objective assessment of psoriasis progression [115,116].

Studies have successfully demonstrated PAI of microvascular lesions in psoriasis, providing a valuable approach to identify and quantitatively measure specific biomarkers for early screening and accurate diagnosis. The PAI of psoriasis biomarkers include elongated and dilated capillary loops, as well as dermal vessels with larger diameters and denser distributions than those in healthy skin (Figure 4b,c) [85,117]. For example, using raster-

scan optoacoustic mesoscopy (RSOM) (Figure 4d,e), PAI studies have revealed correlations between microvascular characteristics and psoriasis response to treatment. Characteristics such as the mean capillary loop length, mean capillary loop diameter, and mean width (thickness) of the sub-epidermal vascular plexus have shown strong associations with treatment outcomes ($r^2 = 0.77$, $p = 0.00004$) [118]. These parameters can be effectively monitored through PAI to capture the therapeutic responses that may elude conventional PASI evaluation [118]. The combination of PAI and OCT has proved mutual corroboration with different scales and depths in dermatitis images [117,119].

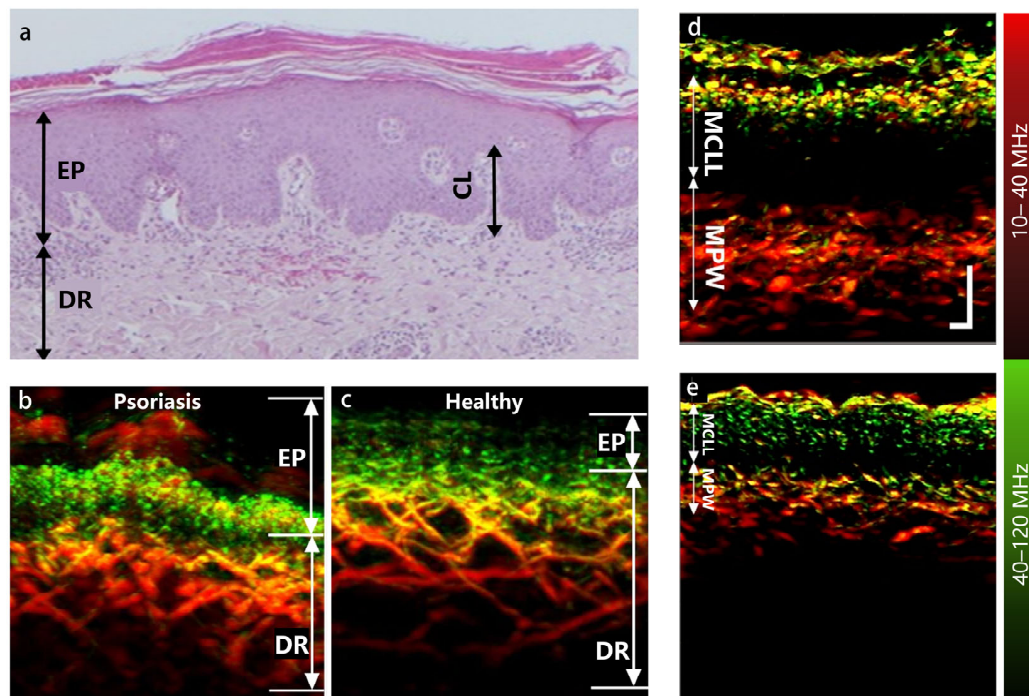


Figure 4. (a) Histological cross section of psoriatic skin showing acanthosis, hyperkeratosis, and elongated capillary loop (CL) [118]. The sub-epidermal vascular plexus appears dilated. (b,c) Cross-sectional MIP images of psoriatic skin and adjacent healthy skin from a patient's back (male) [85]. (d,e) Coronal RSOM images of the same psoriatic plaque on days 1 and 10 of conventional treatment with the PASI 7 and 2. All photoacoustic images are color-coded to represent the two reconstructed frequency bands (red: larger structures in the bandwidth of 10–40 MHz; green: smaller structures in the bandwidth of 40–120 MHz) [118].

3.3. PAI of Some Other Skin Diseases

The imaging of subcutaneous blood oxygen saturation holds significant diagnostic value in hypoxia-associated conditions such as systemic sclerosis and vascular malformations. Systemic sclerosis, characterized by skin fibrosis and progressive vascular involvement, relies primarily on nailfold capillaroscopy for diagnosis (Figure 5a). However, superficial nailfold microvasculature cannot fully represent epidermal conditions. Therefore, RSOM has been used to generate three-dimensional images of the entire nailfold microvascular network that includes dermal vessels (Figure 5b) [120,121]. Multispectral PAI, which is emerging as an important tool for imaging vascular malformations, has also revealed an abnormal increase in arterial blood oxygen saturation (SaO_2) within arteriovenous malformations. Such pathological image features allow PAI to provide crucial insights that may benefit individualized therapy [122].

Diabetes is a condition which affects the microvasculature of various organs, including the eyes, heart, brain, kidneys, and skin [123,124]. The skin is the most accessible organ and could offer a window for detecting diabetes-related systemic effects on the microvasculature. In a study involving 72 diabetic patients, RSOM was employed to image the lower

limbs, and six label-free photoacoustic biomarkers were extracted (Figure 4c) [125,126]. The effects of diabetes on these parameters were investigated as a function of disease severity, finding strong statistically significant differences between microvasculature parameters and diabetes progression. Alterations induced by diabetes in the microvasculature of the skin serve as indicative markers of an unfavorable disease prognosis. These alterations compromise tissue perfusion and oxygenation, as well as the integrity of skin barriers, thereby predisposing individuals to cutaneous infections, neuropathy characterized by sensory loss, ulcerations, and other associated comorbidities such as diabetic foot ulcers [127,128]. PAI holds promise as an effective tool for early detection, potentially transforming the prognosis for this condition [126,129].

Moreover, diabetic foot ulcers are a common and severe complication of type 2 diabetes mellitus, with the potential risk of amputation and even life-threatening consequences arising from persistent ulcers or associated infections [130]. The occurrence of diabetic foot ulcers is intricately linked to microcirculation in the foot, a result of the collective impact of diabetic lower limb neuropathy or peripheral vasculopathy [131]. The dermal vascular system, situated beneath the highly scattering epidermis, remains inaccessible through optical microscopy methods such as confocal or two-photon microscopy. Conventional approaches like ultrasound encounter challenges in visualizing microvessels below the ankle, limiting the assessment of foot microcirculation and impeding the detection of microangiopathy in diabetic foot ulcer patients. PAI, combining the advantages of optical and acoustic techniques with higher resolution and penetration depth, provides a clear observation of the dermal vascular network. He et al. utilized ROSM for the skin imaging of the lower extremities in diabetic participants, resolving skin vessels with diameters ranging from 10 μm to about 150 μm [125]. This capability facilitates quantitative research on biomarkers associated with neuropathy and peripheral vasculopathy. With the progression of diabetes, a reduction in vascular density in the dermal layer and thinning of the epidermis are observed. The high resolution and penetration depth of PAI therefore paves the way for an in-depth exploration of micro-vascular changes relevant to the pathology of diabetic foot ulcers, providing valuable insights for early diagnosis, treatment planning, and preventive strategies.

The potential application landscape of PAI in systemic lupus erythematosus (SLE) is expansive. This imaging modality has proven its value in examining the vasculature [71,85], joints [132,133], and skin injuries [71,83,134], providing a range of insights into the depth and breadth of vascular structural abnormalities, arthritic inflammation, and skin damage. Given the autoimmune nature of SLE, characterized by vascular inflammation similar to psoriasis, PAI assists in observing changes in vascular structure. SLE often presents with joint inflammation, and PAI allows for non-invasive observation of joint structure and inflammation, facilitating early detection and continuous monitoring of disease activity. Furthermore, SLE typically manifests as skin damage, including erythema and ulcers. PAI, with its high-resolution capabilities, provides detailed skin images, assisting physicians in observing the depth and extent of skin lesions. This not only aids in early detection, but also enables more accurate monitoring of pathological changes in SLE, thereby offering robust support for physicians in developing personalized treatment plans. Although PAI is still in the research phase within the lupus erythematosus domain, its unique advantages position it as a powerful tool for future in-depth understanding of autoimmune diseases.

In addition, using only hemoglobin and water as the endogenous contrast, PAI has the potential to characterize the pathological features of healthy skin, superficial dermal burns, deep dermal burns, and deep burns [135]. For acute burns, PAI can clearly delineate the hyperemic bowl, the boundary between the edematous coagulated burned tissue and the healthy perfused tissue [134]. To mitigate the risk of infection and eliminate direct contact with injured skin, non-contact PAI methods have been developed, such as non-contact photoacoustic imaging with focused air-coupled transducers and non-contact photoacoustic imaging using fiber-based interferometers, showing substantial application potential [136,137]. However, non-contact photoacoustic imaging faces challenges related

to reduced signal sensitivity. The necessity for the signal to travel through air or other media may introduce signal attenuation, impacting the imaging sensitivity. Additionally, certain non-contact photoacoustic imaging methods may face limitations concerning the distance the signal travels, particularly when imaging deep tissues. This limitation can lead to lower resolution in deep tissues compared to direct contact methods.

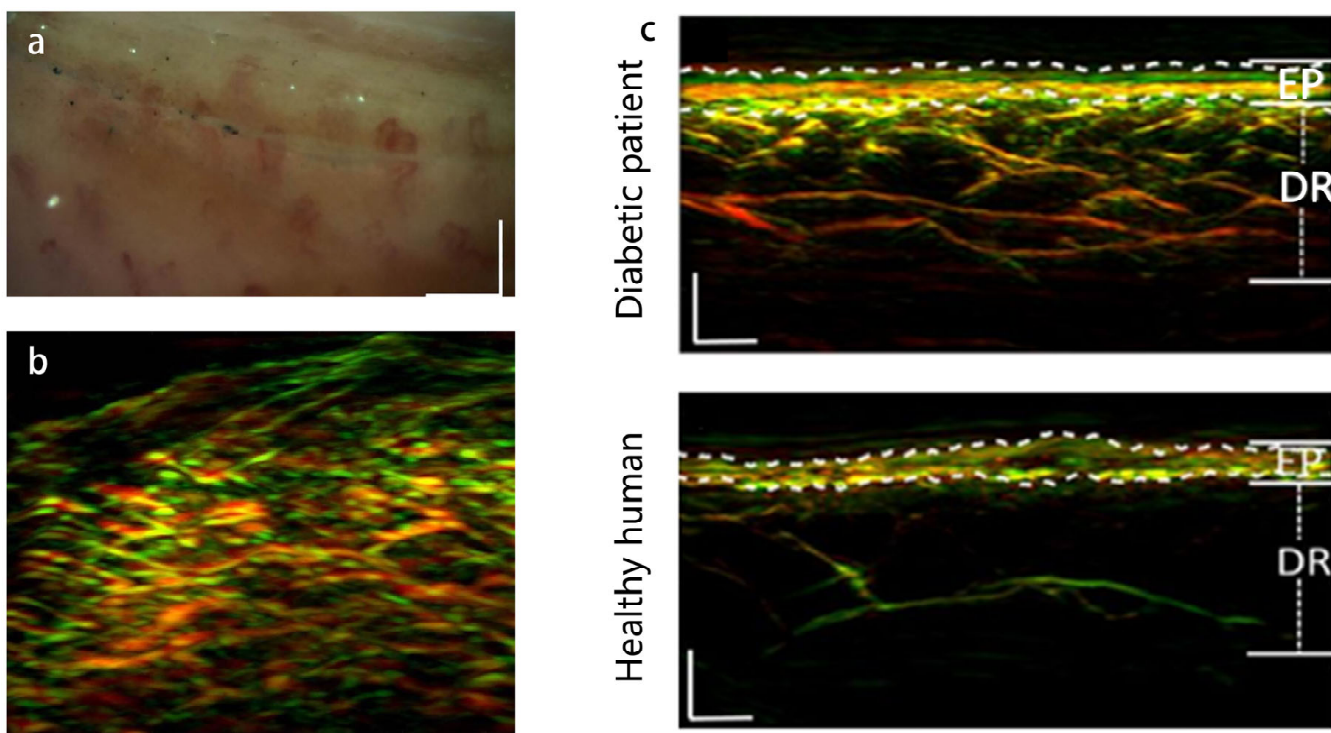


Figure 5. (a) Capillaroscopy image of the nailfold of subject 2 with relatively thick, dark epidermis. The capillaries are barely visible and assessment of vascular morphology is difficult [120]. (b) Maximum intensity projection obtained in the sagittal direction by UWB-RSOM55 of a region in close proximity to the region shown in panel (b) [120]. (c) PAI of lower extremities (distal pretibial region), showing noticeable difference between healthy subjects and diabetic patients [125].

4. Conclusions and Perspective

This review highlights the potential of PAI as a transformative tool for accurate diagnosis and treatment guidance in dermatology. The distinct absorption spectra of biological components acquired using PAI enable the visualization of a wide range of endogenous and exogenous absorbers and provide detailed insights into pathological characteristics. For example, the high imaging contrast of melanin and hemoglobin allows PAI to measure melanoma depth and microvasculature disruption for improved diagnosis. Moreover, PAI can extend to the detection and treatment of circulating melanoma cells, offering a valuable tool for prognosis and personalized treatment. In the context of NMSCs, where accurate measurement of tumor size is critical, PAI shows early promise in accurately distinguishing NMSCs from healthy tissue. In addition to solid tumor imaging, PAI has shown significant benefits in psoriasis diagnosis. Its capability of capturing microvascular alterations in psoriatic skin provides dermatologists a quantitative and objective approach for early screening and accurate diagnosis, offering an improvement over conventional visual assessments. Furthermore, PAI has been demonstrated to measure subcutaneous blood oxygen saturation, offering diagnostic insights into conditions like systemic sclerosis and chronic wounds. The clinical imaging requirement in superficial diseases such as ulcers and diabetes-related lesions further extend the applications of PAI in improving early detection and accurate diagnosis by revealing additional pathological features under the epidermis.

Looking ahead, incorporating advanced techniques such as multiphoton effects and machine learning holds great potential for enhancing PAI's capabilities in skin diagnosis [138–144]. Multiphoton microscopy (MPM), for instance, exploits nonlinear optical effects to achieve subcellular resolution imaging. By integrating multiphoton effects with PAI, the simultaneous visualization of tissue morphology and function at the cellular level within the skin could be achieved. Moreover, this synergy between PAI and MPM could offer clinicians detailed insights into skin structure and function, thereby facilitating early detection and characterization of skin diseases. By combining PAI with other imaging modalities such as ultrasound, Optical Coherence Tomography (OCT), or Raman spectroscopy, clinicians can obtain complementary information about skin anatomy, physiology, and molecular composition, thereby improving diagnostic accuracy for a broad spectrum of skin conditions [138,145–149]. Furthermore, machine learning algorithms can be harnessed to automatically detect and classify skin lesions and assist clinicians in making more accurate diagnoses [139–144]. PAI's ability to provide quantitative measurements of tissue optical properties offers opportunities for identifying novel biomarkers associated with specific skin conditions, further advancing disease diagnosis, prognosis, and treatment monitoring.

While the technical advantages and niche clinical applications of PAI are evident, challenges remain, including the standardization of imaging across diverse patient populations and the establishment of regulatory frameworks for system construction and usage. The translation of PAI from a laboratory technology to a clinical product requires ongoing work to improve reliability, develop expert consensus, and establish clinical guidelines. The recent FDA approval of a PAI system for breast cancer diagnosis exemplifies its growing acceptance in clinical practice and paves the way to additional applications. Overall, the unique advantages and continued development of PAI holds great promise for accurate skin disease diagnosis and treatment management.

Author Contributions: Writing—original draft preparation, Y.Y.; writing—review and editing, Y.Y. and L.L.; supervision, H.Z.; funding acquisition, L.L. and H.Z. All authors have read and agreed to the published version of the manuscript.

Funding: This research was funded by National Research and Development Programme (2022YFC2407700) and State Administration of Traditional Chinese Medicine and Zhejiang Administration of Traditional Chinese Medicine jointly build a science and technology plan project (GZY-ZJ-KJ-2302).

Conflicts of Interest: The authors declare no conflicts of interest.

References

1. Schneider, S.L.; Kohli, I.; Hamzavi, I.H.; Council, M.L.; Rossi, A.M.; Ozog, D.M. Emerging imaging technologies in dermatology. *J. Am. Acad. Dermatol.* **2019**, *80*, 1114–1120. [[CrossRef](#)]
2. Marchetti, M.A.; Cowen, E.A.; Kurtansky, N.R.; Weber, J.; Dauscher, M.; DeFazio, J.; Deng, L.; Dusza, S.W.; Haliasos, H.; Halpern, A.C.; et al. Prospective validation of dermoscopy-based open-source artificial intelligence for melanoma diagnosis (PROVE-AI study). *NPJ Digit. Med.* **2023**, *6*, 127. [[CrossRef](#)]
3. Alenezi, F.; Armghan, A.; Polat, K. A multi-stage melanoma recognition framework with deep residual neural network and hyperparameter optimization-based decision support in dermoscopy images. *Expert Syst. Appl.* **2023**, *215*, 119352. [[CrossRef](#)]
4. Infante, V.H.; Maia Campos, P. Application of a Reflectance Confocal Microscopy Imaging Analysis Score for the Evaluation of NON-MELANOGENIC Changes in Male Photoaged Skin. *Photochem. Photobiol.* **2023**, *99*, 993–1002. [[CrossRef](#)]
5. Perino, F.; Suarez, R.; Perez-Anker, J.; Carrera, C.; Rezze, G.G.; Primiero, C.A.; Alos, L.L.; Diaz, A.; Barreiro, A.; Puig, S.; et al. Concordance of in vivo reflectance confocal microscopy and horizontal-sectioning histology in skin tumours. *Acad. Dermatol. Venereol.* **2024**, *38*, 124–135. [[CrossRef](#)]
6. Cinotti, E.; Brunetti, T.; Cartocci, A.; Tognetti, L.; Suppa, M.; Malvehy, J.; Perez-Anker, J.; Puig, S.; Perrot, J.L.; Rubegni, P. Diagnostic Accuracy of Line-Field Confocal Optical Coherence Tomography for the Diagnosis of Skin Carcinomas. *Diagnostics* **2023**, *13*, 361. [[CrossRef](#)]
7. Kim, H.; Kang, D.; Seong, D.; Saleah, S.A.; Luna, J.A.; Kim, Y.; Kim, H.; Han, S.; Jeon, M.; Kim, J. Skin pore imaging using spectral-domain optical coherence tomography: A case report. *Biomed. Eng. Lett.* **2023**, *13*, 729–737. [[CrossRef](#)]
8. Wortsman, X. Top applications of dermatologic ultrasonography that can modify management. *Ultrasonography* **2023**, *42*, 183–202. [[CrossRef](#)]

9. Alex, A.; Chaney, E.J.; Žurauskas, M.; Criley, J.M.; Spillman, D.R., Jr.; Hutchison, P.B.; Li, J.; Marjanovic, M.; Frey, S.; Arp, Z.; et al. In vivo characterization of minipig skin as a model for dermatological research using multiphoton microscopy. *Exp. Dermatol.* **2020**, *29*, 953–960. [[CrossRef](#)]
10. Marconi, A.; Quadri, M.; Farnetani, F.; Ciardo, S.; Palazzo, E.; Lotti, R.; Cesinaro, A.M.; Fabbiani, L.; Vaschieri, C.; Puviani, M.; et al. In Vivo Melanoma Cell Morphology Reflects Molecular Signature and Tumor Aggressiveness. *J. Investig. Dermatol.* **2022**, *142*, 2205–2216.e6. [[CrossRef](#)]
11. Schmid-Wendtner, M.-H.; Dill-Müller, D. Ultrasound Technology in Dermatology. *Semin. Cutan. Med. Surg.* **2008**, *27*, 44–51. [[CrossRef](#)]
12. Haedicke, K.; Agemy, L.; Omar, M.; Berezhnoi, A.; Roberts, S.; Longo-Machado, C.; Skubal, M.; Nagar, K.; Hsu, H.-T.; Kim, K.; et al. High-resolution optoacoustic imaging of tissue responses to vascular-targeted therapies. *Nat. Biomed. Eng.* **2020**, *4*, 286–297. [[CrossRef](#)]
13. Li, Y.; Wong, T.T.W.; Shi, J.; Hsu, H.-C.; Wang, L.V. Multifocal photoacoustic microscopy using a single-element ultrasonic transducer through an ergodic relay. *Light. Sci. Appl.* **2020**, *9*, 135. [[CrossRef](#)]
14. Wang, L.V.; Yao, J. A practical guide to photoacoustic tomography in the life sciences. *Nat. Methods* **2016**, *13*, 627–638. [[CrossRef](#)]
15. Iskander-Rizk, S.; Visscher, M.; Moerman, A.M.; Korteland, S.-A.; Van Der Heiden, K.; Van Der Steen, A.F.W.; Van Soest, G. Micro Spectroscopic Photoacoustic (μ sPA) imaging of advanced carotid atherosclerosis. *Photoacoustics* **2021**, *22*, 100261. [[CrossRef](#)]
16. Iskander-Rizk, S.; Kruizinga, P.; Beurskens, R.; Springeling, G.; Mastik, F.; De Groot, N.M.S.; Knops, P.; Van Der Steen, A.F.W.; Van Soest, G. Real-time photoacoustic assessment of radiofrequency ablation lesion formation in the left atrium. *Photoacoustics* **2019**, *16*, 100150. [[CrossRef](#)]
17. Li, W.; Sun, X.; Wang, Y.; Niu, G.; Chen, X.; Qian, Z.; Nie, L. In vivo quantitative photoacoustic microscopy of gold nanostar kinetics in mouse organs. *Biomed. Opt. Express* **2014**, *5*, 2679. [[CrossRef](#)]
18. Lv, J.; Xu, Y.; Xu, L.; Nie, L. Quantitative Functional Evaluation of Liver Fibrosis in Mice with Dynamic Contrast-enhanced Photoacoustic Imaging. *Radiology* **2021**, *300*, 89–97. [[CrossRef](#)]
19. Huang, G.; Lv, J.; He, Y.; Yang, J.; Zeng, L.; Nie, L. In vivo quantitative photoacoustic evaluation of the liver and kidney pathology in tyrosinemia. *Photoacoustics* **2022**, *28*, 100410. [[CrossRef](#)]
20. Lin, L.; Hu, P.; Tong, X.; Na, S.; Cao, R.; Yuan, X.; Garrett, D.C.; Shi, J.; Maslov, K.; Wang, L.V. High-speed three-dimensional photoacoustic computed tomography for preclinical research and clinical translation. *Nat. Commun.* **2021**, *12*, 882. [[CrossRef](#)]
21. Attia, A.B.E.; Balasundaram, G.; Moothanchery, M.; Dinish, U.S.; Bi, R.; Ntziachristos, V.; Olivo, M. A review of clinical photoacoustic imaging: Current and future trends. *Photoacoustics* **2019**, *16*, 100144. [[CrossRef](#)]
22. Deán-Ben, X.L.; Fehm, T.F.; Ford, S.J.; Gottschalk, S.; Razansky, D. Spiral volumetric optoacoustic tomography visualizes multi-scale dynamics in mice. *Light. Sci. Appl.* **2017**, *6*, e16247. [[CrossRef](#)]
23. Wang, L.V. Multiscale photoacoustic microscopy and computed tomography. *Nat. Photonics* **2009**, *3*, 503–509. [[CrossRef](#)]
24. Wang, L.V.; Hu, S. Photoacoustic Tomography: In Vivo Imaging from Organelles to Organs. *Science* **2012**, *335*, 1458–1462. [[CrossRef](#)]
25. Lin, L.; Wang, L.V. The emerging role of photoacoustic imaging in clinical oncology. *Nat. Rev. Clin. Oncol.* **2022**, *19*, 365–384. [[CrossRef](#)]
26. Wang, Z.; Yang, F.; Zhang, W.; Xiong, K.; Yang, S. Towards in vivo photoacoustic human imaging: Shining a new light on clinical diagnostics. *Fundam. Res.* **2023**; *in press*. [[CrossRef](#)]
27. Rajendran, P.; Sharma, A.; Pramanik, M. Photoacoustic imaging aided with deep learning: A review. *Biomed. Eng. Lett.* **2022**, *12*, 155–173. [[CrossRef](#)]
28. Liu, W.-W.; Li, P.-C. Photoacoustic imaging of cells in a three-dimensional microenvironment. *J. Biomed. Sci.* **2020**, *27*, 3. [[CrossRef](#)]
29. Chen, Q.; Qin, W.; Qi, W.; Xi, L. Progress of clinical translation of handheld and semi-handheld photoacoustic imaging. *Photoacoustics* **2021**, *22*, 100264. [[CrossRef](#)]
30. Steinberg, I.; Huland, D.M.; Vermesh, O.; Frostig, H.E.; Tummers, W.S.; Gambhir, S.S. Photoacoustic clinical imaging. *Photoacoustics* **2019**, *14*, 77–98. [[CrossRef](#)]
31. Seong, M.; Chen, S.-L. Recent advances toward clinical applications of photoacoustic microscopy: A review. *Sci. China Life Sci.* **2020**, *63*, 1798–1812. [[CrossRef](#)]
32. Hindelang, B.; Aguirre, J.; Schwarz, M.; Berezhnoi, A.; Eyerich, K.; Ntziachristos, V.; Biedermann, T.; Darsow, U. Non-invasive imaging in dermatology and the unique potential of raster-scan optoacoustic mesoscopy. *J. Eur. Acad. Dermatol. Venereol.* **2019**, *33*, 1051–1061. [[CrossRef](#)]
33. Messas, T.; Messas, A.; Kroumpouzos, G. Optoacoustic imaging and potential applications of raster-scan optoacoustic mesoscopy in dermatology. *Clin. Dermatol.* **2022**, *40*, 85–92. [[CrossRef](#)]
34. Von Knorring, T.; Mogensen, M. Photoacoustic tomography for assessment and quantification of cutaneous and metastatic malignant melanoma—A systematic review. *Photodiagnosis Photodyn. Ther.* **2021**, *33*, 102095. [[CrossRef](#)]
35. Li, D.; Humayun, L.; Vienneau, E.; Vu, T.; Yao, J. Seeing through the Skin: Photoacoustic Tomography of Skin Vasculature and Beyond. *JID Innov.* **2021**, *1*, 100039. [[CrossRef](#)]
36. Yao, J.; Wang, L.V. Photoacoustic microscopy: Photoacoustic microscopy. *Laser Photonics Rev.* **2013**, *7*, 758–778. [[CrossRef](#)]
37. Xia, J.; Li, G.; Wang, L.; Nasiriavanaki, M.; Maslov, K.; Engelbach, J.A.; Garbow, J.R.; Wang, L.V. Wide-field two-dimensional multifocal optical-resolution photoacoustic-computed microscopy. *Opt. Lett.* **2013**, *38*, 5236. [[CrossRef](#)]

38. Yao, J.; Song, L.; Wang, L.V. Photoacoustic Microscopy: Superdepth, superresolution, and superb contrast. *IEEE Pulse* **2015**, *6*, 34–37. [[CrossRef](#)]
39. Strohm, E.M.; Berndl, E.S.L.; Kolios, M.C. High frequency label-free photoacoustic microscopy of single cells. *Photoacoustics* **2013**, *1*, 49–53. [[CrossRef](#)] [[PubMed](#)]
40. Xu, G.; Meng, Z.-X.; Lin, J.D.; Yuan, J.; Carson, P.L.; Joshi, B.; Wang, X. The Functional Pitch of an Organ: Quantification of Tissue Texture with Photoacoustic Spectrum Analysis. *Radiology* **2014**, *271*, 248–254. [[CrossRef](#)]
41. Aguirre, J.; Schwarz, M.; Soliman, D.; Buehler, A.; Omar, M.; Ntziachristos, V. Broadband mesoscopic optoacoustic tomography reveals skin layers. *Opt. Lett.* **2014**, *39*, 6297. [[CrossRef](#)] [[PubMed](#)]
42. Jathoul, A.P.; Laufer, J.; Ogunlade, O.; Treeby, B.; Cox, B.; Zhang, E.; Johnson, P.; Pizzey, A.R.; Philip, B.; Marafioti, T.; et al. Deep in vivo photoacoustic imaging of mammalian tissues using a tyrosinase-based genetic reporter. *Nat. Photonics* **2015**, *9*, 239–246. [[CrossRef](#)]
43. Buehler, A.; Deán-Ben, X.L.; Claussen, J.; Ntziachristos, V.; Razansky, D. Three-dimensional optoacoustic tomography at video rate. *Opt. Express* **2012**, *20*, 22712. [[CrossRef](#)] [[PubMed](#)]
44. Mercep, E.; Deán-Ben, X.L.; Razansky, D. Imaging of blood flow and oxygen state with a multi-segment optoacoustic ultrasound array. *Photoacoustics* **2018**, *10*, 48–53. [[CrossRef](#)] [[PubMed](#)]
45. Ivankovic, I.; Mercep, E.; Schmedt, C.-G.; Deán-Ben, X.L.; Razansky, D. Real-time Volumetric Assessment of the Human Carotid Artery: Handheld Multispectral Optoacoustic Tomography. *Radiology* **2019**, *291*, 45–50. [[CrossRef](#)] [[PubMed](#)]
46. Chen, S.-L.; Guo, L.J.; Wang, X. All-optical photoacoustic microscopy. *Photoacoustics* **2015**, *3*, 143–150. [[CrossRef](#)]
47. Hu, S.; Maslov, K.; Wang, L.V. Second-generation optical-resolution photoacoustic microscopy with improved sensitivity and speed. *Opt. Lett.* **2011**, *36*, 1134. [[CrossRef](#)]
48. Lin, L.; Zhang, P.; Xu, S.; Shi, J.; Li, L.; Yao, J.; Wang, L.; Zou, J.; Wang, L.V. Handheld optical-resolution photoacoustic microscopy. *J. Biomed. Opt.* **2016**, *22*, 041002. [[CrossRef](#)]
49. Favazza, C.P.; Wang, L.V.; Jassim, O.W.; Cornelius, L.A. In vivo photoacoustic microscopy of human cutaneous microvasculature and a nevus. *J. Biomed. Opt.* **2011**, *16*, 016015. [[CrossRef](#)]
50. Zhang, H.F.; Maslov, K.; Stoica, G.; Wang, L.V. Functional photoacoustic microscopy for high-resolution and noninvasive in vivo imaging. *Nat. Biotechnol.* **2006**, *24*, 848–851. [[CrossRef](#)] [[PubMed](#)]
51. Qin, W.; Chen, Q.; Xi, L. A handheld microscope integrating photoacoustic microscopy and optical coherence tomography. *Biomed. Opt. Express* **2018**, *9*, 2205. [[CrossRef](#)] [[PubMed](#)]
52. Liu, W.; Shcherbakova, D.M.; Kurupassery, N.; Li, Y.; Zhou, Q.; Verkhusha, V.V.; Yao, J. Quad-mode functional and molecular photoacoustic microscopy. *Sci. Rep.* **2018**, *8*, 11123. [[CrossRef](#)]
53. Zabihian, B.; Weingast, J.; Liu, M.; Zhang, E.; Beard, P.; Pehamberger, H.; Drexler, W.; Hermann, B. In vivo dual-modality photoacoustic and optical coherence tomography imaging of human dermatological pathologies. *Biomed. Opt. Express* **2015**, *6*, 3163. [[CrossRef](#)]
54. Ford, S.J.; Bigliardi, P.L.; Sardella, T.C.P.; Urich, A.; Burton, N.C.; Kacprowicz, M.; Bigliardi, M.; Olivo, M.; Razansky, D. Structural and Functional Analysis of Intact Hair Follicles and Pilosebaceous Units by Volumetric Multispectral Optoacoustic Tomography. *J. Investig. Dermatol.* **2016**, *136*, 753–761. [[CrossRef](#)] [[PubMed](#)]
55. Lin, L.; Hu, P.; Shi, J.; Appleton, C.M.; Maslov, K.; Li, L.; Zhang, R.; Wang, L.V. Single-breath-hold photoacoustic computed tomography of the breast. *Nat. Commun.* **2018**, *9*, 2352. [[CrossRef](#)] [[PubMed](#)]
56. Diot, G.; Metz, S.; Noske, A.; Liapis, E.; Schroeder, B.; Ovsepian, S.V.; Meier, R.; Rummeny, E.; Ntziachristos, V. Multispectral Optoacoustic Tomography (MSOT) of Human Breast Cancer. *Clin. Cancer Res.* **2017**, *23*, 6912–6922. [[CrossRef](#)] [[PubMed](#)]
57. Kothapalli, S.-R.; Sonn, G.A.; Choe, J.W.; Nikoozadeh, A.; Bhuyan, A.; Park, K.K.; Cristman, P.; Fan, R.; Moini, A.; Lee, B.C.; et al. Simultaneous transrectal ultrasound and photoacoustic human prostate imaging. *Sci. Transl. Med.* **2019**, *11*, eaav2169. [[CrossRef](#)]
58. Gargiulo, S.; Albanese, S.; Mancini, M. State-of-the-Art Preclinical Photoacoustic Imaging in Oncology: Recent Advances in Cancer Theranostics. *Contrast Media Mol. Imaging* **2019**, *2019*, 5080267. [[CrossRef](#)] [[PubMed](#)]
59. Deán-Ben, X.L.; Razansky, D. Optoacoustic imaging of the skin. *Exp. Dermatol.* **2021**, *30*, 1598–1609. [[CrossRef](#)] [[PubMed](#)]
60. Upputuri, P.K.; Pramanik, M. Recent advances toward preclinical and clinical translation of photoacoustic tomography: A review. *J. Biomed. Opt.* **2016**, *22*, 041006. [[CrossRef](#)]
61. Regensburger, A.P.; Wagner, A.L.; Claussen, J.; Waldner, M.J.; Knieling, F. Shedding light on pediatric diseases: Multispectral optoacoustic tomography at the doorway to clinical applications. *Mol. Cell Pediatr.* **2020**, *7*, 3. [[CrossRef](#)]
62. Ravina, K.; Lin, L.; Liu, C.Y.; Thomas, D.; Hasson, D.; Wang, L.V.; Russin, J.J. Prospects of Photo- and Thermoacoustic Imaging in Neurosurgery. *Neurosurgery* **2020**, *87*, 11–24. [[CrossRef](#)]
63. Wang, Y.; Thompson, J.M.; Ashbaugh, A.G.; Khodakivsky, P.; Budin, G.; Sinisi, R.; Heinmiller, A.; Van Oosten, M.; Van Dijl, J.M.; Van Dam, G.M.; et al. Preclinical Evaluation of Photoacoustic Imaging as a Novel Noninvasive Approach to Detect an Orthopaedic Implant Infection. *J. Am. Acad. Orthop. Surg.* **2017**, *25*, S7–S12. [[CrossRef](#)]
64. Yao, J.; Wang, L.; Yang, J.-M.; Maslov, K.I.; Wong, T.T.W.; Li, L.; Huang, C.-H.; Zou, J.; Wang, L.V. High-speed label-free functional photoacoustic microscopy of mouse brain in action. *Nat. Methods* **2015**, *12*, 407–410. [[CrossRef](#)] [[PubMed](#)]
65. Lin, L.; Yao, J.; Zhang, R.; Chen, C.; Huang, C.; Li, Y.; Wang, L.; Chapman, W.; Zou, J.; Wang, L.V. High-speed photoacoustic microscopy of mouse cortical microhemodynamics. *J. Biophoton.* **2017**, *10*, 792–798. [[CrossRef](#)] [[PubMed](#)]

66. Stein, E.W.; Maslov, K.; Wang, L.V. Noninvasive, in vivo imaging of blood-oxygenation dynamics within the mouse brain using photoacoustic microscopy. *J. Biomed. Opt.* **2009**, *14*, 020502. [\[CrossRef\]](#) [\[PubMed\]](#)
67. Lan, B.; Liu, W.; Wang, Y.; Shi, J.; Li, Y.; Xu, S.; Sheng, H.; Zhou, Q.; Zou, J.; Hoffmann, U.; et al. High-speed widefield photoacoustic microscopy of small-animal hemodynamics. *Biomed. Opt. Express* **2018**, *9*, 4689. [\[CrossRef\]](#)
68. Rao, A.P.; Bokde, N.; Sinha, S. Photoacoustic Imaging for Management of Breast Cancer: A Literature Review and Future Perspectives. *Appl. Sci.* **2020**, *10*, 767. [\[CrossRef\]](#)
69. Nyayapathi, N.; Xia, J. Photoacoustic imaging of breast cancer: A mini review of system design and image features. *J. Biomed. Opt.* **2019**, *24*, 121911. [\[CrossRef\]](#)
70. Wong, T.T.W.; Zhang, R.; Hai, P.; Zhang, C.; Pleitez, M.A.; Aft, R.L.; Novack, D.V.; Wang, L.V. Fast label-free multilayered histology-like imaging of human breast cancer by photoacoustic microscopy. *Sci. Adv.* **2017**, *3*, e1602168. [\[CrossRef\]](#)
71. Attia, A.B.E.; Chuah, S.Y.; Razansky, D.; Ho, C.J.H.; Malempati, P.; Dinish, U.S.; Bi, R.; Fu, C.Y.; Ford, S.J.; Lee, J.S.-S.; et al. Noninvasive real-time characterization of non-melanoma skin cancers with handheld optoacoustic probes. *Photoacoustics* **2017**, *7*, 20–26. [\[CrossRef\]](#) [\[PubMed\]](#)
72. Stoffels, I.; Morscher, S.; Helffrich, I.; Hillen, U.; Leyh, J.; Burton, N.C.; Sardella, T.C.P.; Claussen, J.; Poepel, T.D.; Bachmann, H.S.; et al. Metastatic status of sentinel lymph nodes in melanoma determined noninvasively with multispectral optoacoustic imaging. *Sci. Transl. Med.* **2015**, *7*, 317ra199. [\[CrossRef\]](#)
73. Zhang, J.; Duan, F.; Liu, Y.; Nie, L. High-Resolution Photoacoustic Tomography for Early-Stage Cancer Detection and Its Clinical Translation. *Radiol. Imaging Cancer* **2020**, *2*, e190030. [\[CrossRef\]](#) [\[PubMed\]](#)
74. Valluru, K.S.; Willmann, J.K. Clinical photoacoustic imaging of cancer. *Ultrasonography* **2016**, *35*, 267–280. [\[CrossRef\]](#) [\[PubMed\]](#)
75. Taruttis, A.; Van Dam, G.M.; Ntziachristos, V. Mesoscopic and Macroscopic Optoacoustic Imaging of Cancer. *Cancer Res.* **2015**, *75*, 1548–1559. [\[CrossRef\]](#)
76. Mehrmohammadi, M.; Joon Yoon, S.; Yeager, D.; Emelianov, S.Y. Photoacoustic Imaging for Cancer Detection and Staging. *Curr. Mol. Imaging* **2013**, *2*, 89–105. [\[CrossRef\]](#)
77. Park, K.; Kim, J.Y.; Lee, C.; Jeon, S.; Lim, G.; Kim, C. Handheld Photoacoustic Microscopy Probe. *Sci. Rep.* **2017**, *7*, 13359. [\[CrossRef\]](#)
78. Na, S.; Russin, J.J.; Lin, L.; Yuan, X.; Hu, P.; Jann, K.B.; Yan, L.; Maslov, K.; Shi, J.; Wang, D.J.; et al. Massively parallel functional photoacoustic computed tomography of the human brain. *Nat. Biomed. Eng.* **2021**, *6*, 584–592. [\[CrossRef\]](#)
79. Kalaora, S.; Nagler, A.; Wargo, J.A.; Samuels, Y. Mechanisms of immune activation and regulation: Lessons from melanoma. *Nat. Rev. Cancer* **2022**, *22*, 195–207. [\[CrossRef\]](#)
80. Schadendorf, D.; van Akkooi, A.C.J.; Berking, C.; Griewank, K.G.; Gutzmer, R.; Hauschild, A.; Stang, A.; Roesch, A.; Ugurel, S. Melanoma. *Lancet* **2018**, *392*, 971–984. [\[CrossRef\]](#)
81. US Preventive Services Task Force; Bibbins-Domingo, K.; Grossman, D.C.; Curry, S.J.; Davidson, K.W.; Ebell, M.; Epling, J.W.; García, F.A.R.; Gillman, M.W.; Kemper, A.R.; et al. Screening for Skin Cancer: US Preventive Services Task Force Recommendation Statement. *JAMA* **2016**, *316*, 429. [\[CrossRef\]](#) [\[PubMed\]](#)
82. Switzer, B.; Puzanov, I.; Skitzki, J.J.; Hamad, L.; Ernstoff, M.S. Managing Metastatic Melanoma in 2022: A Clinical Review. *JCO Oncol. Pract.* **2022**, *18*, 335–351. [\[CrossRef\]](#)
83. Zhou, Y.; Tripathi, S.V.; Rosman, I.; Ma, J.; Hai, P.; Linette, G.P.; Council, M.L.; Fields, R.C.; Wang, L.V.; Cornelius, L.A. Noninvasive Determination of Melanoma Depth using a Handheld Photoacoustic Probe. *J. Investig. Dermatol.* **2017**, *137*, 1370–1372. [\[CrossRef\]](#)
84. Chuah, S.Y.; Attia, A.B.E.; Long, V.; Ho, C.J.H.; Malempati, P.; Fu, C.Y.; Ford, S.J.; Lee, J.S.S.; Tan, W.P.; Razansky, D.; et al. Structural and functional 3D mapping of skin tumours with non-invasive multispectral optoacoustic tomography. *Ski. Res. Technol.* **2017**, *23*, 221–226. [\[CrossRef\]](#)
85. He, H.; Schönmann, C.; Schwarz, M.; Hindelang, B.; Berezhnoi, A.; Steimle-Grauer, S.A.; Darsow, U.; Aguirre, J.; Ntziachristos, V. Fast raster-scan optoacoustic mesoscopy enables assessment of human melanoma microvasculature in vivo. *Nat. Commun.* **2022**, *13*, 2803. [\[CrossRef\]](#)
86. Schadendorf, D.; Fisher, D.E.; Garbe, C.; Gershenwald, J.E.; Grob, J.-J.; Halpern, A.; Herlyn, M.; Marchetti, M.A.; McArthur, G.; Ribas, A.; et al. Melanoma. *Nat. Rev. Dis. Primers* **2015**, *1*, 15003. [\[CrossRef\]](#)
87. Kelly, J.W.; Henderson, M.A.; Thursfield, V.J.; Slavin, J.; Ainslie, J.; Giles, G.G. The management of primary cutaneous melanoma in Victoria in 1996 and 2000. *Med. J. Aust.* **2007**, *187*, 511–514. [\[CrossRef\]](#)
88. Hiemenz, T.J.; Hernández-Irizarry, R.; Boll, J.M.; Jones Coleman, J.E. Accuracy of Diagnostic Biopsy for Cutaneous Melanoma: Implications for Surgical Oncologists. *Int. J. Surg. Oncol.* **2013**, *2013*, 196493. [\[CrossRef\]](#)
89. Ng, J.C.; Swain, S.; Dowling, J.P.; Wolfe, R.; Simpson, P.; Kelly, J.W. The Impact of Partial Biopsy on Histopathologic Diagnosis of Cutaneous Melanoma: Experience of an Australian Tertiary Referral Service. *Arch. Dermatol.* **2010**, *146*, 234–239. [\[CrossRef\]](#)
90. Breathnach, A.; Concannon, E.; Dorairaj, J.J.; Shaharan, S.; McGrath, J.; Jose, J.; Kelly, J.L.; Leahy, M.J. Preoperative measurement of cutaneous melanoma and nevi thickness with photoacoustic imaging. *J. Med. Imaging* **2018**, *5*, 015004. [\[CrossRef\]](#)
91. Zhou, W.; Chen, Z.; Yang, S.; Xing, D. Optical biopsy approach to basal cell carcinoma and melanoma based on all-optically integrated photoacoustic and optical coherence tomography. *Opt. Lett.* **2017**, *42*, 2145. [\[CrossRef\]](#)
92. Zhou, W.; Chen, Z.; Zhou, Q.; Xing, D. Optical Biopsy of Melanoma and Basal Cell Carcinoma Progression by Noncontact Photoacoustic and Optical Coherence Tomography: In Vivo Multi-Parametric Characterizing Tumor Microenvironment. *IEEE Trans. Med. Imaging* **2020**, *39*, 1967–1974. [\[CrossRef\]](#)

93. Omar, M.; Schwarz, M.; Soliman, D.; Symvoulidis, P.; Ntziachristos, V. Pushing the Optical Imaging Limits of Cancer with Multi-Frequency-Band Raster-Scan Optoacoustic Mesoscopy (RSOM). *Neoplasia* **2015**, *17*, 208–214. [[CrossRef](#)]
94. Folkman, J. Role of angiogenesis in tumor growth and metastasis. *Semin. Oncol.* **2002**, *29*, 15–18. [[CrossRef](#)]
95. Weidner, N.; Semple, J.P.; Welch, W.R.; Folkman, J. Tumor Angiogenesis and Metastasis—Correlation in Invasive Breast Carcinoma. *N. Engl. J. Med.* **1991**, *324*, 1–8. [[CrossRef](#)]
96. Hanahan, D.; Weinberg, R.A. Hallmarks of Cancer: The Next Generation. *Cell* **2011**, *144*, 646–674. [[CrossRef](#)]
97. Massagué, J.; Obenauf, A.C. Metastatic colonization by circulating tumour cells. *Nature* **2016**, *529*, 298–306. [[CrossRef](#)]
98. Fidler, I.J. The pathogenesis of cancer metastasis: The “seed and soil” hypothesis revisited. *Nat. Rev. Cancer* **2003**, *3*, 453–458. [[CrossRef](#)]
99. Cristofanilli, M.; Budd, G.T.; Ellis, M.J.; Stopeck, A.; Matera, J.; Miller, M.C.; Reuben, J.M.; Doyle, G.V.; Allard, W.J.; Terstappen, L.W.M.M.; et al. Circulating Tumor Cells, Disease Progression, and Survival in Metastatic Breast Cancer. *N. Engl. J. Med.* **2004**, *351*, 781–791. [[CrossRef](#)]
100. Edgar, R.H.; Tarhini, A.; Sander, C.; Sanders, M.E.; Cook, J.L.; Viator, J.A. Predicting Metastasis in Melanoma by Enumerating Circulating Tumor Cells Using Photoacoustic Flow Cytometry. *Lasers Surg. Med.* **2021**, *53*, 578–586. [[CrossRef](#)] [[PubMed](#)]
101. Shoji, Y.; Bustos, M.A.; Gross, R.; Hoon, D.S.B. Recent Developments of Circulating Tumor Cell Analysis for Monitoring Cutaneous Melanoma Patients. *Cancers* **2022**, *14*, 859. [[CrossRef](#)] [[PubMed](#)]
102. Weight, R.M.; Dale, P.S.; Viator, J.A. Detection of circulating melanoma cells in human blood using photoacoustic flowmetry. In Proceedings of the 2009 Annual International Conference of the IEEE Engineering in Medicine and Biology Society, Minneapolis, MN, USA, 3–6 September 2009; pp. 106–109.
103. Galanzha, E.I.; Menyaev, Y.A.; Yadem, A.C.; Sarimollaoglu, M.; Juratli, M.A.; Nedosekin, D.A.; Foster, S.R.; Jamshidi-Parsian, A.; Siegel, E.R.; Makhoul, I.; et al. In vivo liquid biopsy using Cytophone platform for photoacoustic detection of circulating tumor cells in patients with melanoma. *Sci. Transl. Med.* **2019**, *11*, eaat5857. [[CrossRef](#)] [[PubMed](#)]
104. Hai, P.; Qu, Y.; Li, Y.; Zhu, L.; Shmuylovich, L.; Cornelius, L.A.; Wang, L.V. Label-free high-throughput photoacoustic tomography of suspected circulating melanoma tumor cells in patients in vivo. *J. Biomed. Opt.* **2020**, *25*, 036002. [[CrossRef](#)] [[PubMed](#)]
105. He, Y.; Wang, L.; Shi, J.; Yao, J.; Li, L.; Zhang, R.; Huang, C.-H.; Zou, J.; Wang, L.V. In vivo label-free photoacoustic flow cytography and on-the-spot laser killing of single circulating melanoma cells. *Sci. Rep.* **2016**, *6*, 39616. [[CrossRef](#)] [[PubMed](#)]
106. Watts, C.; Price, S.J.; Santarius, T. Current Concepts in the Surgical Management of Glioma Patients. *Clin. Oncol.* **2014**, *26*, 385–394. [[CrossRef](#)]
107. Etzkorn, J.R.; Alam, M. What Is Mohs Surgery? *JAMA Dermatol.* **2020**, *156*, 716. [[CrossRef](#)]
108. Folkman, J. Angiogenesis in cancer, vascular, rheumatoid and other disease. *Nat. Med.* **1995**, *1*, 27–30. [[CrossRef](#)]
109. Carmeliet, P.; Jain, R.K. Angiogenesis in cancer and other diseases. *Nature* **2000**, *407*, 249–257. [[CrossRef](#)]
110. Plumb, A.A.; Huynh, N.T.; Guggenheim, J.; Zhang, E.; Beard, P. Rapid volumetric photoacoustic tomographic imaging with a Fabry-Perot ultrasound sensor depicts peripheral arteries and microvascular vasomotor responses to thermal stimuli. *Eur. Radiol.* **2018**, *28*, 1037–1045. [[CrossRef](#)]
111. Chen, Z.; Rank, E.; Meiburger, K.M.; Sinz, C.; Hodul, A.; Zhang, E.; Hoover, E.; Minneman, M.; Ensher, J.; Beard, P.C.; et al. Non-invasive multimodal optical coherence and photoacoustic tomography for human skin imaging. *Sci. Rep.* **2017**, *7*, 17975. [[CrossRef](#)]
112. Ron, A.; Deán-Ben, X.L.; Gottschalk, S.; Razansky, D. Volumetric Optoacoustic Imaging Unveils High-Resolution Patterns of Acute and Cyclic Hypoxia in a Murine Model of Breast Cancer. *Cancer Res.* **2019**, *79*, 4767–4775. [[CrossRef](#)]
113. Greb, J.E.; Goldminz, A.M.; Elder, J.T.; Lebwohl, M.G.; Gladman, D.D.; Wu, J.J.; Mehta, N.N.; Finlay, A.Y.; Gottlieb, A.B. Psoriasis. *Nat. Rev. Dis. Primers* **2016**, *2*, 16082. [[CrossRef](#)]
114. Branisteanu, D.E.; Cojocaru, C.; Diaconu, R.; Porumb, E.A.; Alexa, A.I.; Nicolescu, A.C.; Brihan, I.; Bogdanici, C.M.; Branisteanu, G.; Dimitriu, A.; et al. Update on the etiopathogenesis of psoriasis (Review). *Exp. Ther. Med.* **2022**, *23*, 201. [[CrossRef](#)] [[PubMed](#)]
115. Griffiths, C.E.; Barker, J.N. Pathogenesis and clinical features of psoriasis. *Lancet* **2007**, *370*, 263–271. [[CrossRef](#)]
116. Ryan, C.; Korman, N.J.; Gelfand, J.M.; Lim, H.W.; Elmets, C.A.; Feldman, S.R.; Gottlieb, A.B.; Koo, J.Y.M.; Lebwohl, M.; Leonardi, C.L.; et al. Research gaps in psoriasis: Opportunities for future studies. *J. Am. Acad. Dermatol.* **2014**, *70*, 146–167. [[CrossRef](#)] [[PubMed](#)]
117. Aguirre, J.; Schwarz, M.; Garzorz, N.; Omar, M.; Buehler, A.; Eyerich, K.; Ntziachristos, V. Precision assessment of label-free psoriasis biomarkers with ultra-broadband optoacoustic mesoscopy. *Nat. Biomed. Eng.* **2017**, *1*, 0068. [[CrossRef](#)]
118. Hindelang, B.; Nau, T.; Englert, L.; Berezhnoi, A.; Lauffer, F.; Darsow, U.; Biedermann, T.; Eyerich, K.; Aguirre, J.; Ntziachristos, V. Enabling precision monitoring of psoriasis treatment by optoacoustic mesoscopy. *Sci. Transl. Med.* **2022**, *14*, eabm8059. [[CrossRef](#)]
119. Ossadnik, K.; Philipp, S.; Bost, W.; Fournelle, M.; Richter, H.; Lademann, J. Application of Photoacoustic Methods and Confocal Microscopy for Monitoring of Therapeutic Response in Plaque Psoriasis. *Ski. Pharmacol. Physiol.* **2018**, *31*, 308–315. [[CrossRef](#)] [[PubMed](#)]
120. Aguirre, J.; Hindelang, B.; Berezhnoi, A.; Darsow, U.; Lauffer, F.; Eyerich, K.; Biedermann, T.; Ntziachristos, V. Assessing nailfold microvascular structure with ultra-wideband raster-scan optoacoustic mesoscopy. *Photoacoustics* **2018**, *10*, 31–37. [[CrossRef](#)]
121. Hofstee, H.M.A.; Serné, E.H.; Roberts, C.; Hesselstrand, R.; Scheja, A.; Moore, T.L.; Wildt, M.; Manning, J.B.; Vonk Noordegraaf, A.; Voskuyl, A.E.; et al. A multicentre study on the reliability of qualitative and quantitative nail-fold videocapillaroscopy assessment. *Rheumatology* **2012**, *51*, 749–755. [[CrossRef](#)]

122. Masthoff, M.; Helfen, A.; Claussen, J.; Karlas, A.; Markwardt, N.A.; Ntziachristos, V.; Eisenblätter, M.; Wildgruber, M. Use of Multispectral Optoacoustic Tomography to Diagnose Vascular Malformations. *JAMA Dermatol.* **2018**, *154*, 1457. [CrossRef] [PubMed]
123. Barrett, E.J.; Liu, Z.; Khamaisi, M.; King, G.L.; Klein, R.; Klein, B.E.K.; Hughes, T.M.; Craft, S.; Freedman, B.I.; Bowden, D.W.; et al. Diabetic Microvascular Disease: An Endocrine Society Scientific Statement. *J. Clin. Endocrinol. Metab.* **2017**, *102*, 4343–4410. [CrossRef] [PubMed]
124. Cheung, C.Y.; Ikram, M.K.; Klein, R.; Wong, T.Y. The clinical implications of recent studies on the structure and function of the retinal microvasculature in diabetes. *Diabetologia* **2015**, *58*, 871–885. [CrossRef] [PubMed]
125. He, H.; Fasoula, N.-A.; Karlas, A.; Omar, M.; Aguirre, J.; Lutz, J.; Kallmayer, M.; Füchtenbusch, M.; Eckstein, H.-H.; Ziegler, A.; et al. Opening a window to skin biomarkers for diabetes stage with optoacoustic mesoscopy. *Light Sci. Appl.* **2023**, *12*, 231. [CrossRef] [PubMed]
126. Karlas, A.; Katsouli, N.; Fasoula, N.-A.; Bariotakis, M.; Chlis, N.-K.; Omar, M.; He, H.; Iakovakis, D.; Schäffer, C.; Kallmayer, M.; et al. Dermal features derived from optoacoustic tomograms via machine learning correlate microangiopathy phenotypes with diabetes stage. *Nat. Biomed. Eng.* **2023**, *7*, 1667–1682. [CrossRef] [PubMed]
127. Greenman, R.L.; Panasyuk, S.; Wang, X.; Lyons, T.E.; Dinh, T.; Longoria, L.; Giurini, J.M.; Freeman, J.; Khaodhia, L.; Veves, A. Early changes in the skin microcirculation and muscle metabolism of the diabetic foot. *Lancet* **2005**, *366*, 1711–1717. [CrossRef] [PubMed]
128. Caballero, A.E.; Arora, S.; Saouaf, R.; Lim, S.C.; Smakowski, P.; Park, J.Y.; King, G.L.; LoGerfo, F.W.; Horton, E.S.; Veves, A. Microvascular and macrovascular reactivity is reduced in subjects at risk for type 2 diabetes. *Diabetes* **1999**, *48*, 1856–1862. [CrossRef]
129. Mennes, O.A.; van Netten, J.J.; Slart, R.H.J.A.; Steenbergen, W. Novel Optical Techniques for Imaging Microcirculation in the Diabetic Foot. *Curr. Pharm. Des.* **2018**, *24*, 1304–1316. [CrossRef]
130. McDermott, K.; Fang, M.; Boulton, A.J.M.; Selvin, E.; Hicks, C.W. Etiology, Epidemiology, and Disparities in the Burden of Diabetic Foot Ulcers. *Diabetes Care* **2023**, *46*, 209–221. [CrossRef]
131. Huang, F.; Lu, X.; Yang, Y.; Yang, Y.; Li, Y.; Kuai, L.; Li, B.; Dong, H.; Shi, J. Microenvironment-Based Diabetic Foot Ulcer Nanomedicine. *Adv. Sci.* **2023**, *10*, 2203308. [CrossRef]
132. Wang, Z.; Tong, Z.; Chen, H.; Nie, G.; Hu, J.; Liu, W.; Wang, E.; Yuan, B.; Wang, Z.; Hu, J. Photoacoustic/ultrasonic dual-mode imaging for monitoring angiogenesis and synovial erosion in rheumatoid arthritis. *Photoacoustics* **2023**, *29*, 100458. [CrossRef]
133. Peng, X.; Xu, Z.; Dentinger, A.; Kewalramani, S.; Jo, J.; Xu, G.; Chamberland, D.; Abdulaziz, N.; Gandikota, G.; Mills, D.; et al. Longitudinal volumetric assessment of inflammatory arthritis via photoacoustic imaging and Doppler ultrasound imaging. *Photoacoustics* **2023**, *31*, 100514. [CrossRef] [PubMed]
134. Zhang, H.F.; Maslov, K.; Stoica, G.; Wang, L.V. Imaging acute thermal burns by photoacoustic microscopy. *J. Biomed. Opt.* **2006**, *11*, 054033. [CrossRef] [PubMed]
135. Yamazaki, M.; Sato, S.; Ashida, H.; Saito, D.; Okada, Y.; Obara, M. Measurement of burn depths in rats using multiwavelength photoacoustic depth profiling. *J. Biomed. Opt.* **2005**, *10*, 064011. [CrossRef] [PubMed]
136. Hochreiner, A.; Bauer-Marschallinger, J.; Burgholzer, P.; Jakoby, B.; Berer, T. Non-contact photoacoustic imaging using a fiber based interferometer with optical amplification. *Biomed. Opt. Express* **2013**, *4*, 2322–2331. [CrossRef] [PubMed]
137. Deán-Ben, X.L.; Pang, G.A.; Montero de Espinosa, F.; Razansky, D. Non-contact optoacoustic imaging with focused air-coupled transducers. *Appl. Phys. Lett.* **2015**, *107*, 051105. [CrossRef]
138. Song, W.; Xu, Q.; Zhang, Y.; Zhan, Y.; Zheng, W.; Song, L. Fully integrated reflection-mode photoacoustic, two-photon and second harmonic generation microscopy in vivo. *Sci. Rep.* **2016**, *6*, 32240. [CrossRef] [PubMed]
139. Chen, X.; Qi, W.; Xi, L. Deep-learning-based motion-correction algorithm in optical resolution photoacoustic microscopy. *Vis. Comput. Ind. Biomed. Art* **2019**, *2*, 12. [CrossRef] [PubMed]
140. Zhao, H.; Ke, Z.; Yang, F.; Li, K.; Chen, N.; Song, L.; Zheng, C.; Liang, D.; Liu, C. Deep Learning Enables Superior Photoacoustic Imaging at Ultralow Laser Dosages. *Adv. Sci.* **2021**, *8*, 2003097. [CrossRef]
141. Li, J.; Wang, C.; Chen, T.; Lu, T.; Li, S.; Sun, B.; Gao, F.; Ntziachristos, V. Deep learning-based quantitative optoacoustic tomography of deep tissues in the absence of labeled experimental data. *Optica* **2022**, *9*, 32. [CrossRef]
142. Li, X.; Zhang, S.; Wu, J.; Huang, S.; Feng, Q.; Qi, L.; Chen, W. Multispectral Interlaced Sparse Sampling Photoacoustic Tomography. *IEEE Trans. Med. Imaging* **2020**, *39*, 3463–3474. [CrossRef]
143. Wang, G.; Ye, J.C.; De Man, B. Deep learning for tomographic image reconstruction. *Nat. Mach. Intell.* **2020**, *2*, 737–748. [CrossRef]
144. Chen, Y.; Xu, C.; Zhang, Z.; Zhu, A.; Xu, X.; Pan, J.; Liu, Y.; Wu, D.; Huang, S.; Cheng, Q. Prostate cancer identification via photoacoustic spectroscopy and machine learning. *Photoacoustics* **2021**, *23*, 100280. [CrossRef]
145. Forbrich, A.; Heinmiller, A.; Zemp, R.J. Photoacoustic imaging of lymphatic pumping. *J. Biomed. Opt.* **2017**, *22*, 106003. [CrossRef] [PubMed]
146. Toi, M.; Asao, Y.; Matsumoto, Y.; Sekiguchi, H.; Yoshikawa, A.; Takada, M.; Kataoka, M.; Endo, T.; Kawaguchi-Sakita, N.; Kawashima, M.; et al. Visualization of tumor-related blood vessels in human breast by photoacoustic imaging system with a hemispherical detector array. *Sci. Rep.* **2017**, *7*, 41970. [CrossRef] [PubMed]
147. Hosseinaee, Z.; Tummon Simmons, J.A.; Reza, P.H. Dual-Modal Photoacoustic Imaging and Optical Coherence Tomography [Review]. *Front. Phys.* **2021**, *8*, 616618. [CrossRef]

148. Park, J.; Park, B.; Kim, T.Y.; Jung, S.; Choi, W.J.; Ahn, J.; Yoon, D.H.; Kim, J.; Jeon, S.; Lee, D.; et al. Quadruple ultrasound, photoacoustic, optical coherence, and fluorescence fusion imaging with a transparent ultrasound transducer. *Proc. Natl. Acad. Sci. USA* **2021**, *118*, e1920879118. [[CrossRef](#)] [[PubMed](#)]
149. Rao, B.; Soto, F.; Kerschensteiner, D.; Wang, L.V. Integrated photoacoustic, confocal, and two-photon microscope. *J. Biomed. Opt.* **2014**, *19*, 036002. [[CrossRef](#)] [[PubMed](#)]

Disclaimer/Publisher's Note: The statements, opinions and data contained in all publications are solely those of the individual author(s) and contributor(s) and not of MDPI and/or the editor(s). MDPI and/or the editor(s) disclaim responsibility for any injury to people or property resulting from any ideas, methods, instructions or products referred to in the content.